Observer-based high-order sliding mode control of DFIG-based wind energy conversion systems subjected to sensor faults

Mousavi , Yashar; Bevan, Geraint; Kucukdemiral, ibrahim Beklan; Fekih, Afef

Published in:
IEEE Transactions on Industry Applications

DOI:
10.1109/TIA.2023.3317823

Publication date:
2024

Document Version
Author accepted manuscript

Observer-based High-order Sliding Mode Control of DFIG-based Wind Energy Conversion Systems Subjected to Sensor Faults

Yashar Mousavi, Geraint Bevan, Ibrahim Beklan Küçükdemiral, and Afef Fekih

August 21, 2023

Abstract

Recent advances in technology have paved the way for the increased penetration of wind energy conversion systems (WECSs) into the grid, worldwide. However, the existence of model uncertainties and intermittency of wind power can lead to malfunction of the stabilizing controllers and degrade the WECSs' power production performance. In this work, a compound control scheme comprising active fault-tolerant fractional-order nonsingular terminal sliding mode controllers (AFTSMCs) and a sliding mode observer (SMO) is developed to enhance the robustness of doubly-fed induction generator (DFIG) -based WECSs against uncertainties and maintain their desired performance. The developed AFTSMCs alleviate the chattering problem and overcome the compromise between fast response and the undesirable chattering problem. At the same time, it performs the speed trajectory tracking and rotor current regulation tasks. Moreover, under inevitable false fault detections due to unavoidable gradual performance degradations in the current sensors, a tolerance boundary is circumscribed for actual faults occurrence, allowing the developed robust SMO to estimate and reconstruct the rotor current during sensor faults with a high level of reliability. Evaluations of comparative performance are provided and validate the cooperative fault-tolerant method's superior control performance over other advanced approaches.

Keywords: Wind turbine, Fault-tolerant control, Higer-order sliding mode control, Sliding mode observer, Sensor faults.

1 Introduction

Over the past decade, significant attention has been paid to wind energy-based power production, prompting an increase in wind energy conversion systems (WECSs) installations on offshore and onshore farms. However, the intermittent characteristics of wind power impose a considerable challenge to grid power regulation, which demands the reliable operation of WECSs in a variety of wind conditions. In this context, benefiting from the emerging developments of controlled power converters, the

Nomenclature

AFTSMC	Active fractional-order nonsingular terminal SMC
DFIG	Doubly-fed induction generator
GSC	Grid side converter
PWM	Pulse width modulation
RSC	Rotor side converter
SMC	Sliding mode control
SMO	Sliding mode observer
WECS	Wind energy conversion systems
WT	Wind turbine
Wind turbine model	
P_a	Aerodynamic power
ρ	Air density
R	Rotor radius
C_P	Power coefficient
$C_{p,\max}$	Maximum power coefficient
β	Blade pitch angle
β_{opt}	Blade maximum pitch angle
υ	Effective wind speed
ρ	Air density
λ	Tip-speed ratio
Ω_r, Ω_t	Generator and shaft mechanical speed
T_r, T_t	Generator and aerodynamic torque
T_{em}	Electromagnetic torque
N_g	Gear ratio
$P_{grid-ref}$	Grid reference power
$\bar{\eta}$	Wind turbine efficiency
$\mathcal{V}_{ds}, \mathcal{V}_{qs}, \mathcal{V}_{dr}, \mathcal{V}_{qr}$	d-axis and q-axis voltage components
$v_{s\alpha}, v_{s\beta}$	Voltage in the stator reference frame
$\mathcal{I}_{ds}, \mathcal{I}_{qs}, \mathcal{I}_{dr}, \mathcal{I}_{qr}$	d-axis and q-axis current components
$\mathcal{L}_m$	Magnetizing inductance
$\mathcal{L}_r, \mathcal{L}_m$	Stator and rotor inductances
$\mathcal{R}_r, \mathcal{R}_s$	Rotor and stator resistances
$\varphi_{ds}, \varphi_{qs}, \varphi_{dr}, \varphi_{qr}$	Stator and rotor flux components
$\varphi_{s\alpha}, \varphi_{s\beta}$	Flux linkage in the stator reference frame
ω_s, ω_r	Stator and rotor angular speeds
N_P	Number of pole pairs
P_s, Q_s	Active and reactive powers at the stator
s	Generator slip
d	Unknown lumped uncertainty
Controller and Observer	
γ	Fractional derivation order
$\beta_i, \kappa_i, \eta_i, i = 1, 2, ..., 6$	Controllers' arbitrary auxiliary scalars
$S_{1,2,3}$	Controllers' sliding surfaces
ξ^*	Slowly varying lumped disturbance
ς	Observer's sliding surface
$h(\varsigma)$	Sigmoid function
a	Observer's arbitrary auxiliary positive scalar
$\mathcal{N}$	Auxiliary constant positive matrix
$M, Q, J, \mathcal{P}$	Positive definite auxiliary matrices
$\Re$	The rotor current measurement error
Q	Estimation tolerance boundary

doubly-fed induction generator (DFIG) -based configuration has overtaken other con-

figurations due to the expanded controllability with regard to independent active and reactive power controls, variable speed operation, low-cost, and high efficiency [1, 2].

The DFIG comprises two power converters, the rotor-side and the grid-side (RSC and GSC). The rotor winding is supplied via a back-to-back pulse width modulation (PWM) based voltage source converter, and the stator is directly connected to the grid. The RSC maintains the active and reactive power flow between the DFIG and the grid. In terms of controlling the power converters, several techniques have been proposed to control the RSC of DFIG, such as backstepping control [3], machine learning-based control [4], event-triggered robust control [5], feedback linearization-based PI control [6], model predictive control [7, 8], and fuzzy control [9]. However, despite the desired control performance of the approaches mentioned above in preserving the continuous operation of WECSs, their sensitivity to parameter uncertainties and external disturbances has led to a gradual investigation of more efficient methods during the past decade.

On the other hand, sliding mode control (SMC) approaches have been emerging as advanced control strategies with remarkable control performance because of their merits, such as insensitivity to parametric and unmodeled uncertainties and delivering rapid responses [2]. Particularly, while the system is subjected to uncertainties and disturbances, the SMC can determine absolute tracking precision with developed sliding surfaces and reaching laws. For a DFIG-based WECS affected by parametric uncertainties, authors in [10] proposed a power point tracking SMC control scheme. The developed scheme comprised a cascade control loop for DC-link voltage regulation and a rotor current controller. Later in [11], an augmentation of the feedback linearization method and SMC was developed for RSC control of DFIG-based wind turbines (WTs).

However, even though conventional SMC approaches have shown acceptable performance in controlling WECSs, their main problems, such as the chattering phenomenon and large control signals production still persist, especially when the WECS is subjected to inevitable faults, uncertainties, and disturbances [2, 12]. As a result, various research works have tried to diminish the problems by developing more reliable control schemes [13]. As one solution, soft computing techniques such as neural network SMC and fuzzy SMC have been found to be effective methodologies with reduced chattering and disturbance rejection characteristics [14–17]. However, further improvements to the control structure are required to achieve an ideal sliding motion and deliver the desired performance. On the other hand, fractional-order and higher-order SMC approaches have successfully emerged as reliable alternatives with outstanding performance in respect of guaranteed fast finite-time convergence, alleviated chattering, higher control precision, and robust performance against external disturbances and model uncertainties [2, 12, 18–21]. In the sense of converter control of DFIG-driven WTs, an adaptive fractional-order terminal SMC (FTSMC) approach was developed in [22]. As reported, integrating the fractional concept with the terminal sliding surface could effectively mitigate the chattering and deliver a desirable performance. In [23], the RSC control of DFIG-based WECS was addressed via a fast adaptive TSMC considering diverse and challenging situations. In another study [4], the recurrent high-order neural network trained with the extended Kalman filter was developed to build up the DFIG models. Then, a super-twisting-based higher-order

high-order SMC with reduced chattering was synthesized to improve the quality of the generated power. Authors in [24] proposed a second-order SMC with mitigated chattering for RSC control of WECSs subjected to unknown disturbances and parametric uncertainties.

A critical issue is that the WECSs' current control relies heavily on the rotor and stator currents' measurements. In other words, the reliability and performance of the WECS degrade in case of any failure in the sensor(s) in providing the required measurements. Accordingly, a wide variety of methods have been available for detecting and isolating faults, both model-based and signal-based [25–28]. Authors in [20] proposed an observer-based FTSMC scheme for the RSC control of WECSs subjected to rotor current sensor faults and model uncertainties. They used the algebraic state observer [28] for the rotor current estimation, while the estimation process could still be enhanced to deliver less error. In another study [25], sliding mode observers were proposed to estimate the WT generator-induced speed, rotor speed, and aerodynamic torque. However, despite the acceptable performance of the designed observers in normal conditions, their performance was drastically affected by wind speed variations. Accordingly, the sudden variations of wind speeds, a normal phenomenon in real-world applications, resulted in undesired performance reductions in the developed observers. Authors in [27] developed a sliding mode perturbation and state observer to aggregate the parameter uncertainties of WECS. However, although the developed estimation approach's performance was reported as satisfactory, some minor smooth faults have been considered in the performance investigations. Hence, the method's application in practice, where the inevitable faults can affect the system, is yet to be investigated to validate its performance.

This work proposes an active fault-tolerant FTSMC (AFTSMC) paradigm to control the RSC of DFIG-driven WTs. Its main contributions are as follows:

- Two AFTSMC approaches with mitigated chattering and guaranteed finite-time convergence for the speed trajectory tracking and rotor current regulation of DFIG-based WECSs.
- A robust sliding mode observer (SMO) to accurately and reliably estimate and reconstruct the rotor current during sensor faults.
- A design that considers a tolerance boundary to minimize the false fault detections resulting from the unavoidable gradual performance degradation in the current sensors.
- A comparative performance assessment with FSMC [29] and algebraic state-observer-based FTSMC [20] approaches.

The remainder of the paper is organized as follows. Section 2 presents the DFIG-based WT. The proposed active fault-tolerant controllers together with the developed SMO are investigated in Section 3. Simulations and performance investigations are illustrated in Section 4, and the paper concludes with Section 5.

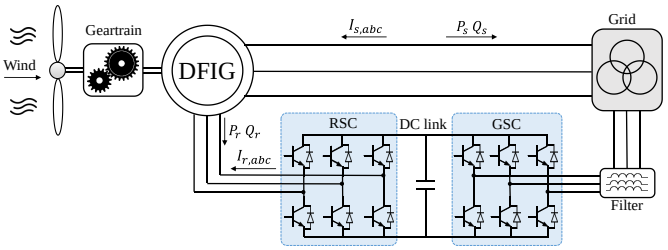

Figure 1: Schematic diagram of a DFIG-based wind power system.

2 Modeling of DFIG-based WT

WTs convert the aerodynamic wind power into rotational energy and electrical power. Figure 2 shows the schematic diagram of a DFIG-based wind power system. The aerodynamic power is defined as

$$P_a = \frac{1}{2}\rho\pi R^2 \upsilon^3 C_P\Big(\lambda,\beta\Big), \tag{1}$$

where υ [m/s], ρ [kg/m^3], and R [m] denote the wind speed, air density, and rotor radius, respectively.

The power coefficient C_P is usually obtained with respect to the tip-speed ratio $\lambda = R\Omega_t/\upsilon$ and the pitch angle β [rad], where Ω_t [rad/sec] denotes the shaft's mechanical speed [2].

Given the generator speed $\Omega_r = \Omega_t T_t$, the WT generator torque can be expressed as $T_r = \Omega_r/N_g$, where T_t is the aerodynamic torque and N_g denotes the gear ratio. Accordingly, the grid power and reference rotor speed can be expressed as

$$P_{grid-ref} = \frac{1}{2}\bar{\eta}\rho\pi^2 C_{p-max}\upsilon^3, \tag{2}$$

$$\Omega_{r-ref} = \frac{\lambda_{opt} N_g}{R}\upsilon, \tag{3}$$

where $\bar{\eta}$ represents the WT efficiency and $C_{P,\max} \triangleq C_P(\beta_{opt}, \lambda_{opt})$ represents the maximum C_P obtained in respect of the optimum values of tip-speed ratio λ_{opt} and pitch angle β_{opt}.

In a synchronously rotating $d-q$ frame, the DFIG-based WT model can be expressed as [30]:

$$\mathcal{V}_{ds} = \mathcal{R}_s \mathcal{I}_{ds} + \frac{d}{dt}\varphi_{ds} - \omega_s \varphi_{qs}, \tag{4a}$$

$$\mathcal{V}_{qs} = \mathcal{R}_s \mathcal{I}_{qs} + \frac{d}{dt}\varphi_{qs} - \omega_s \varphi_{ds}, \tag{4b}$$

$$\mathcal{V}_{dr} = \mathcal{R}_r \mathcal{I}_{ds} + \frac{d}{dt}\varphi_{dr} - (\omega_s - \omega_r)\,\varphi_{qr}, \tag{4c}$$

$$\mathcal{V}_{qr} = \mathcal{R}_r \mathcal{I}_{qs} + \frac{d}{dt}\varphi_{qr} + (\omega_s - \omega_r)\,\varphi_{dr}, \tag{4d}$$

based on the flux equations of the stator and rotor as

$$\varphi_{ds} = \mathcal{L}_m \mathcal{I}_{dr} + \mathcal{L}_s \mathcal{I}_{ds}, \tag{5a}$$
$$\varphi_{qs} = \mathcal{L}_m \mathcal{I}_{qr} + \mathcal{L}_s \mathcal{I}_{qs}, \tag{5b}$$
$$\varphi_{dr} = \mathcal{L}_m \mathcal{I}_{ds} + \mathcal{L}_r \mathcal{I}_{dr}, \tag{5c}$$
$$\varphi_{qr} = \mathcal{L}_m \mathcal{I}_{qs} + \mathcal{L}_r \mathcal{I}_{qr}, \tag{5d}$$

where the subscripts s and r stand for the stator and rotor, respectively. $\left\{\mathcal{V}_{ds}, \mathcal{V}_{qs}\right\}$ and $\left\{\mathcal{V}_{dr}, \mathcal{V}_{qr}\right\}$ denote the d-axis and q-axis voltage components in [V], $\left\{\mathcal{I}_{ds}, \mathcal{I}_{qs}\right\}$ and $\left\{\mathcal{I}_{dr}, \mathcal{I}_{qr}\right\}$ represent the current components in [A]. $\mathcal{L}_m$ is the magnetizing inductance in [H], and $\mathcal{L}_r$ and $\mathcal{L}_m$ are the stator and rotor inductances, respectively. $\mathcal{R}_r$ and $\mathcal{R}_s$ are the rotor and stator resistances in [Ω]. $\left\{\varphi_{ds}, \varphi_{qs}\right\}$ and $\left\{\varphi_{dr}, \varphi_{qr}\right\}$ are the stator and rotor flux components in [Wb], respectively. ω_s [rad/s] and $\omega_r = N_P \Omega_r$ denote the stator and rotor angular speeds, respectively, with N_P being the number of pole pairs.

The rotating components' dynamics can be manifested as $J\dot{\Omega}_r = T_{em} - T_r - f_r \Omega_r$, with J being the moment of inertia of the rotating components and f_r representing the friction coefficient. The electromagnetic torque T_{em} can be given as

$$T_{em} = N_P \frac{\mathcal{L}_m}{\mathcal{L}_s} \left(\varphi_{qs} \mathcal{I}_{dr} - \varphi_{ds} \mathcal{I}_{qr}\right). \tag{6}$$

Aligning the reference frame with the d-axis of the stator flux φ_s results in $\varphi_{ds} = \varphi_s$, $\varphi_{qs} = 0$, and

$$T_{em} = N_P \frac{\mathcal{L}_m \mathcal{V}_s}{\omega_s \mathcal{L}_s} \mathcal{I}_{qr}. \tag{7}$$

Neglecting the stator resistance per phase one has $\mathcal{V}_{ds} = 0$ and $\mathcal{V}_{qs} = \mathcal{V}_s = \omega_s \varphi_s$. Hence, the voltage at the rotor and the power at the stator can be represented as

$$\mathcal{V}_{dr} = \mathcal{R}_r \mathcal{I}_{dr} - \sigma \mathcal{L}_r s \omega_s \mathcal{I}_{qr} + \sigma \mathcal{L}_r \frac{d}{dt} \mathcal{I}_{dr}, \tag{8a}$$
$$\mathcal{V}_{qr} = \mathcal{R}_r \mathcal{I}_{qr} - \sigma s \omega_s \mathcal{I}_{dr} + s \frac{\mathcal{L}_m \mathcal{V}_s}{\mathcal{L}_s} + \sigma \mathcal{L}_r \frac{d}{dt} \mathcal{I}_{qr}, \tag{8b}$$

$$P_s = -\frac{\mathcal{L}_m \mathcal{V}_s}{\mathcal{L}_s} \mathcal{I}_{qr}, \tag{9a}$$
$$Q_s = \frac{\mathcal{V}_s^2}{\omega_s \mathcal{L}_s} - \frac{\mathcal{L}_m \mathcal{V}_s}{\mathcal{L}_s} \mathcal{I}_{dr}, \tag{9b}$$

where $s = (\omega_s - \omega_r)/\omega_s$ represents the generator slip and $\sigma = 1 - \mathcal{L}_m/(\mathcal{L}_r \mathcal{L}_s)$.

Considering (4)-(9), the nonlinear system model can be obtained as

$$\dot{x} = \mathcal{Z}(x) + \mathcal{Y} u \cong \hat{z}(x) + \hat{y} u + d, \tag{10}$$

where $u = [\mathcal{V}_{dr}\ \mathcal{V}_{qr}]^T$ represents the control signal, $x = [\mathcal{I}_{dr}\ \mathcal{I}_{qr}]^T$ is the state vector, and the best approximations of $\mathcal{Z}(x)$ and $\mathcal{Y}$ are denoted as

$$\hat{z}(x) = \begin{bmatrix} -\frac{\mathcal{R}_r}{\sigma\mathcal{L}_r}\mathcal{I}_{dr} + s\omega_s\mathcal{I}_{qr} \\ -\frac{\mathcal{R}_r}{\sigma\mathcal{L}_r}\mathcal{I}_{qr} - s\omega_s\mathcal{I}_{dr} + s\frac{\mathcal{L}_m\mathcal{V}_s}{\sigma\mathcal{L}_r\mathcal{L}_s} \end{bmatrix}, \tag{11a}$$

$$\hat{y} = (\sigma\mathcal{L}_r)^{-1} I_{2\times2}, \tag{11b}$$

where $I_{2\times2}$ is an identity matrix. Here, $d = \Delta\hat{z} + \Delta\hat{y}u = [d_1\ d_2]^T$ is the unknown lumped uncertainty, with $\Delta\hat{y}$ and $\Delta\hat{z}(x)$ being the input and model uncertainties, respectively.

3 Fault-Tolerant Controller Design

The proposed fault-tolerant SMO-based AFTSMC scheme for the RSC of DFIG-based WT is investigated in this section. Accordingly, an AFTSMC approach is developed to regulate the rotor current, whereas a second AFTSMC approach is derived for the speed trajectory tracking. For the sake of simplicity, the time-dependence is omitted from the equations.

3.1 Current Control

Given the reference trajectory defined as $x_{ref} = \left[\mathcal{I}_{dr-ref}\ \ \mathcal{I}_{qr-ref}\right]^T$ and (7), the active power reference can be represented by:

$$\mathcal{I}_{qr-ref} = \frac{\omega_s\mathcal{L}_s}{N_P\mathcal{L}_m\mathcal{V}_s}T_{em-ref}. \tag{12}$$

Note that T_{em-ref} will later be provided by the speed controller (Section 3.2).

Remark 1. *The reactive power reference can be defined as*

$$Q_{s-ref} = \frac{\mathcal{V}_s^2}{\omega_s\mathcal{L}_s} - \frac{\mathcal{L}_m\mathcal{V}_s}{\mathcal{L}_s}\mathcal{I}_{dr}. \tag{13}$$

However, Q_{s-ref} is set to zero ($Q_{s-ref} = 0$) to obtain an improved power factor.

Therefore, considering (13), one achieves

$$\mathcal{I}_{dr-ref} = \mathcal{V}_s/\omega_s\mathcal{L}_m. \tag{14}$$

Considering (10) the tracking error dynamics $\dot{e} = \dot{x} - \dot{x}_{ref}$ can be obtained as

$$\dot{e} = \hat{z}(x) + \hat{y}u + d - \dot{x}_{ref}, \tag{15}$$

Hence, the AFTSMC sliding surface is proposed as

$$S = \begin{bmatrix} S_1 \\ S_2 \end{bmatrix} = \begin{bmatrix} \kappa_1 e_1 + \kappa_2\mathfrak{D}^{\gamma-1}e_1 + \frac{1}{\beta_1}\mathfrak{D}^{\gamma}|e_1|^{\frac{p_1}{q_1}} \\ \kappa_3 e_2 + \kappa_4\mathfrak{D}^{\gamma-1}e_2 + \frac{1}{\beta_2}\mathfrak{D}^{\gamma}|e_2|^{\frac{p_2}{q_2}} \end{bmatrix}, \tag{16}$$

where $\beta_i > 0, \kappa_i > 0, i = 1, 2$ are arbitrary scalars, $\mathfrak{D}^{\gamma}(\cdot)$ denotes the Riemann-Liouville fractional derivation of order $0 < \gamma < 1$, and p_i and q_i are odd positive scalars that satisfy $1 < (p_i/q_i) < 2, i = 1, 2$.

Taking the time-derivative of (16) yields

$$\dot{S} = \begin{bmatrix} \dot{S}_1 \\ \dot{S}_2 \end{bmatrix} = \begin{bmatrix} \kappa_1 \dot{e}_1 + \kappa_2 \mathfrak{D}^{\gamma} e_1 + \frac{p_1}{\beta_1 q_1} \mathfrak{D}^{\gamma} |e_1|^{\frac{p_1}{q_1} - 1} \\ \kappa_3 \dot{e}_2 + \kappa_4 \mathfrak{D}^{\gamma} e_2 + \frac{p_2}{\beta_2 q_2} \mathfrak{D}^{\gamma} |e_2|^{\frac{p_2}{q_2} - 1} \end{bmatrix}, \tag{17}$$

Note that

$$\dot{e} = \begin{bmatrix} \dot{e}_1 \\ \dot{e}_2 \end{bmatrix} = \begin{bmatrix} \hat{z}(x) + \hat{y} u_1 + d_1 - \dot{I}_{dr-ref} \\ \hat{z}(x) + \hat{y} u_2 + d_2 - \dot{I}_{qr-ref} \end{bmatrix}. \tag{18}$$

Then, substituting (18) into (17) yields

$$\dot{S} = \begin{bmatrix} \kappa_1 \left(\hat{z}(x) + \hat{y} u_1 + d_1 - \dot{I}_{dr-ref} \right) + \kappa_2 \mathfrak{D}^{\gamma} e_1 + \frac{p_1}{\beta_1 q_1} \mathfrak{D}^{\gamma} |e_1|^{\frac{p_1}{q_1} - 1} \\ \kappa_3 \left(\hat{z}(x) + \hat{y} u_2 + d_2 - \dot{I}_{qr-ref} \right) + \kappa_4 \mathfrak{D}^{\gamma} e_2 + \frac{p_2}{\beta_2 q_2} \mathfrak{D}^{\gamma} |e_2|^{\frac{p_2}{q_2} - 1} \end{bmatrix}. \tag{19}$$

Hence, one can formulate the control law as follows

$$\underbrace{\begin{bmatrix} u_1 \\ u_2 \end{bmatrix}}_{u} = \begin{bmatrix} \hat{y}^{-1} \kappa_1^{-1} \left(-\hat{z}(x) - d_1 + \dot{I}_{dr-ref} - \kappa_2 \mathfrak{D}^{\gamma} e_1 - \frac{p_1}{\beta_1 q_1} \mathfrak{D}^{\gamma} |e_1|^{\frac{p_1}{q_1} - 1} \right) \\ \hat{y}^{-1} \kappa_3^{-1} \left(-\hat{z}(x) - d_2 + \dot{I}_{qr-ref} - \kappa_4 \mathfrak{D}^{\gamma} e_2 - \frac{p_2}{\beta_2 q_2} \mathfrak{D}^{\gamma} |e_2|^{\frac{p_2}{q_2} - 1} \right) \end{bmatrix}. \tag{20}$$

Given the equivalent control law as

$$u_{eq} = u + u_{sw}, \tag{21}$$

the effects of the lumped uncertainties are compensated by u_{sw}, defined as

$$\underbrace{\begin{bmatrix} u_{sw,1} \\ u_{sw,2} \end{bmatrix}}_{u_{sw}} = \begin{bmatrix} -\kappa_1^{-1} \left(\eta_1 \mathsf{sgn}(S_1) + \eta_2 S_1 \right) \\ -\kappa_3^{-1} \left(\eta_3 \mathsf{sgn}(S_2) + \eta_4 S_2 \right) \end{bmatrix}, \tag{22}$$

where $\eta_i > 0$ is an arbitrary scalar and $\mathsf{sgn}(\cdot)$ represents the signum function.

Theorem 1. *Considering the sliding surface* (16) *and the equivalent control* u_{eq}*, the dynamics of the tracking error converge to the sliding surface and then asymptotically converge to zero in finite time.*

Proof. Consider the Lyapunov function candidate

$$V = \frac{1}{2} S^2. \tag{23}$$

Differentiating V with respect to time and substituting (16) and (19) yields:

$$\begin{aligned}\underbrace{\begin{bmatrix}\dot{V}_1\\ \dot{V}_2\end{bmatrix}}_{\dot{V}} &= \begin{bmatrix}S_1\dot{S}_1\\ S_2\dot{S}_2\end{bmatrix} \\ &= \begin{bmatrix}-S_1\left(\eta_1\mathsf{sgn}\left(S_1\right)+\eta_2 S_1\right)\\ -S_2\left(\eta_3\mathsf{sgn}\left(S_2\right)+\eta_4 S_2\right)\end{bmatrix} \\ &\leq \begin{bmatrix}-\eta_1\left|S_1\right|-\eta_2 S_1^2\\ -\eta_3\left|S_2\right|-\eta_4 S_2^2\end{bmatrix} \\ &\leq \begin{bmatrix}0\\ 0\end{bmatrix}.\end{aligned} \tag{24}$$

Hence, the system's states converge to $S = 0$ asymptotically.

To investigate the finite-time convergence, let us rewrite (24) and take into consideration of $S^2 = 2V$ as follows:

$$\dot{V} = \begin{bmatrix}dV_1/dt_1\\ dV_2/dt_2\end{bmatrix} = \begin{bmatrix}-\eta_1\left|\sqrt{2V_1}\right|-2\eta_2 V_1\\ -\eta_3\left|\sqrt{2V_2}\right|-2\eta_4 V_2\end{bmatrix}. \tag{25}$$

From (25) and defining $b \triangleq 1/2$, one obtains

$$\begin{aligned}\begin{bmatrix}dV_1/dt_1\\ dV_2/dt_2\end{bmatrix} &\leq \begin{bmatrix}-\frac{dV_1}{\sqrt{2}\eta_1\sqrt{V_1}+2\eta_2 V_1}\\ -\frac{dV_2}{\sqrt{2}\eta_3\sqrt{V_2}+2\eta_4 V_2}\end{bmatrix} \\ &\leq \begin{bmatrix}-\frac{dV_1}{2^b\eta_1 V_1^b+2\eta_2 V_1}\\ -\frac{dV_2}{2^b\eta_3 V_2^b+2\eta_4 V_2}\end{bmatrix} \\ &\leq \begin{bmatrix}-\frac{V_1^{-b}dV_1}{2^b\eta_1+2\eta_2 V_1^{b-1}}\\ -\frac{V_2^{-b}dV_2}{2^b\eta_3+2\eta_4 V_2^{b-1}}\end{bmatrix} \\ &\leq \begin{bmatrix}-\frac{dV_1^{1-b}}{(1-b)\left(2^b\eta_1+2\eta_2 V_1^{b-1}\right)}\\ -\frac{dV_2^{1-b}}{(1-b)\left(2^b\eta_3+2\eta_4 V_2^{b-1}\right)}\end{bmatrix}.\end{aligned} \tag{26}$$

Solving (26) results in the convergence time as

$$\begin{aligned}\begin{bmatrix}t_{s,1}-t_{r,1}\\ t_{s,2}-t_{r,2}\end{bmatrix} &\leq \begin{bmatrix}-\frac{1}{2\eta_2(1-b)}\int_{V_1(t_{r,1})}^{V_1(t_{s,1})}\frac{dV_1^{1-b}}{\frac{2^b\eta_1}{2\eta_2}+V_1^{1-b}}\\ -\frac{1}{2\eta_4(1-b)}\int_{V_2(t_{r,2})}^{V_2(t_{s,2})}\frac{dV_2^{1-b}}{\frac{2^b\eta_3}{2\eta_4}+V_2^{1-b}}\end{bmatrix} \\ &\leq \begin{bmatrix}\frac{1}{2\eta_2(2-b)}\ln\left(V_1^{1-b}+\frac{2^b\eta_1}{2\eta_2}\right)_{V_1(t_{r,1})}^{V_1(t_{s,1})}\\ \frac{1}{2\eta_4(2-b)}\ln\left(V_2^{1-b}+\frac{2^b\eta_3}{2\eta_4}\right)_{V_2(t_{r,2})}^{V_2(t_{s,2})}\end{bmatrix},\end{aligned} \tag{27}$$

where $V_0\left(t_{s,i}\right) = 0$, and $t_{r,i}$ and $t_{s,i}$ represent the reaching and settling time, respectively.

As a consequence, the system states converge to zero at the following finite times, when the system acts on the sliding surface (16):

$$\begin{bmatrix} t_{s,1} \\ t_{s,2} \end{bmatrix} \leq \begin{bmatrix} \frac{1}{2\eta_2(2-b)} \ln\left(V_1^{1-b}(t_{r,1}) + \frac{2^b\eta_1}{2\eta_2}\right) + (t_{r,1}) \\ \frac{1}{2\eta_4(2-b)} \ln\left(V_2^{1-b}(t_{r,2}) + \frac{2^b\eta_3}{2\eta_4}\right) + (t_{r,2}) \end{bmatrix}. \tag{28}$$

□

3.2 Speed Control

The mechanical dynamics of the system can be defined as

$$\dot{\Omega}_r = \frac{T_{em}}{J} + d_3, \tag{29}$$

where T_{em} denotes the control input, and the lumped uncertainty is represented by $d_3 = -\frac{T_r}{J} - \frac{f_r\Omega_r}{J}$. Considering $e_3 = \Omega_r - \Omega_{r-ref}$ as the speed tracking error and substituting its dynamics $\dot{e}_3 = \dot{\Omega}_r - \dot{\Omega}_{r-ref}$ into (29), one obtains

$$\dot{e}_3 = \frac{T_{em}}{J} + d_3 - \dot{\Omega}_{r-ref}. \tag{30}$$

The sliding surface S_3 is proposed as

$$S_3 = \kappa_5 e_3 + \kappa_6 \mathfrak{D}^{\gamma-1} e_3 + \frac{1}{\beta_3} \mathfrak{D}^{\gamma} |e_3|^{\frac{p_3}{q_3}}, \tag{31}$$

where p_3 and q_3 are odd positive scalars that satisfy $1 < (p_3/q_3) < 2$.

The time derivative of (31) along the error dynamics (30) yields

$$\dot{S}_3 = \kappa_5 \left(\frac{T_{em}}{J} + d_3 - \dot{\Omega}_{r-ref}\right) + \kappa_6 \mathfrak{D}^{\gamma} e_3 + \frac{p_3}{\beta_3 q_3} \mathfrak{D}^{\gamma} |e_3|^{\frac{p_3}{q_3}-1}. \tag{32}$$

The speed control law can be derived from (32) as follows

$$T_{em} = J\kappa_5^{-1} \left(-d_3 + \dot{\Omega}_{r-ref} - \kappa_6 \mathfrak{D}^{\gamma} e_3 - \frac{p_3}{\beta_3 q_3} \mathfrak{D}^{\gamma} |e_3|^{\frac{p_3}{q_3}-1}\right). \tag{33}$$

Defining the switching control law as

$$T_{em,sw} = -\kappa_5^{-1} \left(\eta_5 \mathsf{sgn}\left(S_3\right) + \eta_6 S_3\right), \tag{34}$$

allows us to write the equivalent control law as $T_{em,eq} = T_{em} + T_{em,sw}$.

For the purpose of stability analysis, let us consider the Lyapunov function candidate as $V_3 = S_3^2/2$. Substituting (32) and $T_{em,eq}$ in the time derivative of V_3, one gets

$$\begin{aligned} \dot{V}_3 &= S_3 \dot{S}_3 \\ &= -S_3 \left(\eta_5 \mathsf{sgn}\left(S_3\right) + \eta_6 S_3\right) \\ &\leq -\eta_5 \left|S_3\right| - \eta_6 S_3^2 \\ &\leq 0. \end{aligned} \tag{35}$$

Hence, the system states are thus asymptotically converged to the sliding surface. The finite time convergence investigation is similar to the one described in Section 3.1, and yields

$$t_{s,3} \leq \frac{1}{2\eta_6 (2-b)} \ln\left(V_3^{1-b}(t_{r,3}) + \frac{2^b \eta_5}{2\eta_6}\right) + (t_{r,3}). \tag{36}$$

Remark 2. *Considering* (28) *and* (36)*, one can observe that defining* $\eta_2 \gg \eta_1$*,* $\eta_4 \gg \eta_3$*, and* $\eta_6 \gg \eta_5$ *can deliver less convergence time of the system states to zero. However, the parameters must be chosen properly to avoid unwanted perturbations being imposed on the system.*

4 Sliding Mode Observer Design

The practical current control of WECSs requires measuring the rotor current. However, in the absence of accurate measurements, the accuracy of the control system and, consequently, its reliability and performance would be compromised. Accordingly, a robust sliding mode observer is developed to estimate and reconstruct the rotor current in the $d-q$ reference frame during sensor faults.

Assumption 1. *The system is subjected to slowly varying lumped disturbance* $\xi^* = \Delta\mathcal{A}\mathcal{I} + \Delta\mathcal{B}\mathcal{V} + \Delta\mathcal{D}\mathcal{V}_s + d$*, that satisfies the Lipschitz condition* $\|\xi^* - \hat{\xi}^*\| \leq \bar{J}\|\mathcal{I} - \hat{\mathcal{I}}\|$*, where* $\bar{J}$ *is a positive scalar.*

Assumption 2. *It is assumed that a positive constant* χ *exists such that satisfies* $\|\xi^*\| \leq \chi$*.*

Considering Assumption 1, (8) can be rewritten as

$$\dot{\mathcal{I}} = \mathcal{A}_n\mathcal{I} + \mathcal{B}_n\mathcal{V} + \mathcal{D}_n\mathcal{V}_s + \xi^* \tag{37}$$

where $\mathcal{I} = [\mathcal{I}_{dr} \;\; \mathcal{I}_{qr}]^T$, $\mathcal{V} = [\mathcal{V}_{dr} \;\; \mathcal{V}_{qr}]^T$, and

$$\mathcal{A}_n = \begin{bmatrix} -\frac{\mathcal{R}_r}{\sigma\mathcal{L}_r} & s\omega_s \\ \frac{s\omega_s}{\mathcal{L}_r} & -\frac{\mathcal{R}_r}{\sigma\mathcal{L}_r} \end{bmatrix}, \mathcal{B}_n = \begin{bmatrix} \frac{1}{\sigma\mathcal{L}_r} & \frac{1}{\sigma\mathcal{L}_r} \end{bmatrix}^T,$$
$$\mathcal{D}_n = \begin{bmatrix} 0 & -\frac{s\mathcal{L}_m}{\sigma\mathcal{L}_r\mathcal{L}_s} \end{bmatrix}^T.$$

Chattering occurs when the signum function is used as the switching function in an SMO. As a result, in order to estimate the back EMF, the output of the SMO must first pass through the low pass filter (LPF), which adds a delay and necessitates additional compensation for the calculation of the rotor position. On the other hand, chattering imposes some fluctuations in the steady-state response. This occurs notably when there are significant differences in the estimated parameters in the high-speed region. Accordingly, the observer gain needs to be increased to limit the significant variations that can lead to uncontrollable circumstances [31]. In order to eliminate the undesirable chattering, a sigmoid function is used in this research as the switching function, which requires neither an LPF nor an extra compensator for the position of the rotor. The

gains of the implemented SMO are selected heuristically to satisfy the sliding mode condition by pushing the system states onto the sliding surface, providing robustness against uncertainties.

The SMO is designed as

$$\dot{\hat{\mathcal{I}}} = \mathcal{A}_n \hat{\mathcal{I}} + \mathcal{B}_n \mathcal{V} + \mathcal{D}_n \mathcal{V}_s + \mathcal{N} h(\varsigma) + \hat{\xi}^*, \tag{38}$$

where $\varsigma = \mathcal{I} - \hat{\mathcal{I}}$ is the observer's sliding surface and $\hat{\mathcal{I}} = [\hat{\mathcal{I}}_{dr} \;\; \hat{\mathcal{I}}_{qr}]^T$ denotes the estimated values of $\mathcal{I}_{dr}, \mathcal{I}_{qr}$. $h(\varsigma)$ is a sigmoid function defined as $h(\varsigma) = 2/(1 + e^{-a\varsigma}) - 1$, $a > 0$ is a scalar used to regulate the slope of the sigmoid function, and $\mathcal{N}$ is a constant positive matrix with appropriate dimension.

Subtracting (37) from (38), the error dynamic equation of the SMO can be obtained as follows

$$\dot{\tilde{\mathcal{I}}} = \mathcal{A}_n \tilde{\mathcal{I}} - \mathcal{N} h(\varsigma) + \tilde{\xi}^*, \tag{39}$$

where $\tilde{\mathcal{I}} = e = \mathcal{I} - \hat{\mathcal{I}}$ denotes the estimation error, and $\tilde{\xi}^* = \xi^* - \hat{\xi}^*$.

Lemma 1. *[32] Positive definite matrices M and Q with proper dimensions exist, satisfying*

$$M^T Q + Q^T M \leq \zeta M^T M + \zeta^{-1} Q^T Q. \tag{40}$$

where $\zeta > 0$ is a auxiliary scalar.

Lemma 2. *[32] Given the positive definite matrix J and $\mathcal{A}_n$ being Hurwitz, the positive definite matrix $\mathcal{P}$ exists, satisfying*

$$\mathcal{A}_n^T \mathcal{P} + \mathcal{P} \mathcal{A}_n + \mu J^T J + \mu^{-1} \mathcal{P}^2 < 0. \tag{41}$$

where $\mu > 0$ is a auxiliary scalar.

Theorem 2. *Given an appropriate matrix $\mathcal{N}$ satisfying $\|\mathcal{N}\| = \|\xi\|$ yields the asymptotical stability of the error dynamic* (39)*.*

Proof. Consider the Lyapunov function candidate as

$$V_4 = e^T \mathcal{P} e. \tag{42}$$

The time-dependant derivation of (42) yields

$$\dot{V}_4 = e^T \left(\mathcal{A}_n^T \mathcal{P}\right) e - 2 e^T \mathcal{N} h(e) + \tilde{\xi}^{*T} \mathcal{P} e + e^T \mathcal{P} \tilde{\xi}^*. \tag{43}$$

From Lemma 2 one obtains

$$\begin{aligned} \tilde{\xi}^{*T} \mathcal{P} e + e^T \mathcal{P} \tilde{\xi}^* &\leq \mu \tilde{\xi}^{*T} \tilde{\xi}^* + \mu^{-1} e^T \mathcal{P}^2 e \\ &= \mu \tilde{\xi}^{*2} + \mu^{-1} e^T \mathcal{P}^2 e \leq \mu J^2 \|\tilde{\xi}^*\| + \mu^{-1} e^T \mathcal{P}^2 e \\ &= e^T \left(\mu J^T J + \mu^{-1} \mathcal{P}^2\right) e. \end{aligned} \tag{44}$$

Defining $\Psi = e^T \left(\mathcal{A}_n^T \mathcal{P}\right) e + \tilde{\xi}^{*T} \mathcal{P} e + e^T \mathcal{P} \tilde{\xi}^*$ for the sake of simplification. one can obtain

$$\Psi \leq e^T \left(\mathcal{A}_n^T \mathcal{P}\right) e + e^T \left(\mu J^T J + \mu^{-1} \mathcal{P}^2\right) e < 0, \tag{45}$$

which results in $\dot{V}_4 = \Psi - 2e^T \mathcal{N} h(e) < 0$. Accordingly, the locally bounded stability of the error system (39) is achieved, and the developed SMO can perform the rotor currents estimation. □

Let the difference between the measured and the estimated rotor current in the $d-q$ reference frame be represented as $\Re = |\tilde{I}|$. Flawlessly, $\Re = 0$ and $\Re > 0$ should denote the no-fault and faulty circumstances, respectively. However, due to the unavoidable performance degradation of current sensors over time, false fault detections are inevitable, which can violate the above assumption in practice. To avoid this issue, a tolerance boundary Q can be circumscribed for actual faults occurrence, where $\Re > Q$ and $\Re \leq Q$ illustrate the faulty and no-fault circumstances, respectively. As a result, the developed SMO can estimate and reconstruct the rotor current during sensors' faults.

The flux linkage and voltage can be expressed in the stator reference frame as

$$\begin{cases} \varphi_{s\alpha} = \mathcal{L}_s i_{s\alpha} + \mathcal{L}_m i_{r\alpha}, \\ \varphi_{s\beta} = \mathcal{L}_s i_{s\beta} + \mathcal{L}_m i_{r\beta}, \end{cases} \tag{46}$$

$$\begin{cases} v_{s\alpha} = \mathcal{R}_s i_{s\alpha} + \dot{\varphi}_{s\alpha}, \\ v_{s\beta} = \mathcal{R}_s i_{s\beta} + \dot{\varphi}_{s\beta}. \end{cases}$$

Considering the time derivative of (46) in (47) yields,

$$\dot{i}_{r\alpha} = \frac{1}{\mathcal{L}_m} v_{s\alpha} - \frac{\mathcal{R}_s}{\mathcal{L}_m} i_{s\alpha} - \frac{\mathcal{L}_s}{\mathcal{L}_m} \dot{i}_{s\alpha}, \tag{47a}$$

$$\dot{i}_{r\beta} = \frac{1}{\mathcal{L}_m} v_{s\beta} - \frac{\mathcal{R}_s}{\mathcal{L}_m} i_{s\beta} - \frac{\mathcal{L}_s}{\mathcal{L}_m} \dot{i}_{s\beta}. \tag{47b}$$

Considering (47), the rotor current can be approximated in $\alpha - \beta$ frame as

$$\hat{i}_{r\alpha} = \frac{1}{\mathcal{L}_m} \int v_{s\alpha} - \frac{\mathcal{R}_s}{\mathcal{L}_m} \int i_{s\alpha} - \frac{\mathcal{L}_s}{\mathcal{L}_m} i_{s\alpha}, \tag{48a}$$

$$\hat{i}_{r\beta} = \frac{1}{\mathcal{L}_m} \int v_{s\beta} - \frac{\mathcal{R}_s}{\mathcal{L}_m} \int i_{s\beta} - \frac{\mathcal{L}_s}{\mathcal{L}_m} i_{s\beta}. \tag{48b}$$

As apparent from (48), the approximations of rotor current are dependant on the stator currents and voltage measurements. As a result, if $\Re > Q$, the current control law u_{eq} (21) is derived from the rotor current approximation (48). Figure **??** illustrates the block diagram of the proposed fault-tolerant control schemes.

5 Simulation Results

The effectiveness of the proposed SMO-based fault-tolerant AFTSMC scheme for the speed trajectory tracking and rotor current regulation of a 1.5 MW DFIG-based WT is tested with respect to FSMC [29] and algebraic state-observer-based FTSMC [20] approaches through simulations in the MATLAB/Simulink platform with the following specifications: MATLAB R2021b 64-bit, on a DELL laptop with 64-bit win10 operating system, processor: Intel® core™ i7-10875U CPU 2.30 GHz, installed memory:

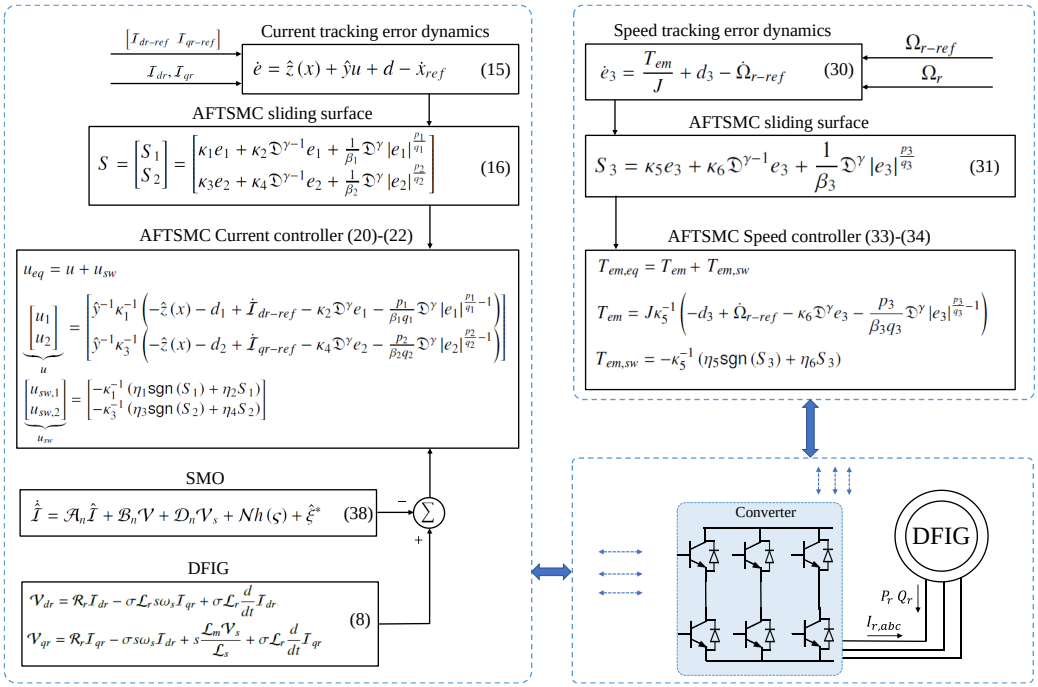

Figure 2: Schematic diagram of the proposed fault-tolerant control scheme.

Table 1: System characteristics.

Parameter	Value	Unit
Nominal power	1.5	MW
Rated wind speed	11	m/s
Operating range	4-30	m/s
Generator rated voltage	575	v
Generator stator resistance	0.023	pu
Generator stator inductance	0.18	pu
Generator inertia constant	0.685	s
Gearbox ratio	62.5	–
Air density	1.225	kg/m^3
Nominal DC-link voltage	1150	v
DC bus capacitor	10	mf

64.00 GB. Table 1 illustrates the system characteristics. Parametric uncertainties and sensor faults are considered to affect the WT. In this respect, the system is considered to be affected by the lumped disturbance $d = 50\%f + 50\%hu$. At the same time, multiple fault occurrences are assumed to happen during the time intervals of 35-50s and 120-140s for $\mathcal{I}_{dr}$, and 15-35s, 65-75s, and 150-170s for $\mathcal{I}_{qr}$ while evaluating the controllers. The imposed faults are stemmed from experimental behavior, *i.e.*, a sudden step-like change with semi-sinusoidal fluctuations at the endpoint, to be added to the $d-q$ currents, changing the currents' values. The parameters and gain of the SMO are chosen as $\bar{J} = 1e-9$, $\mathcal{N} = [1.2\ 0; 0\ 1.2]$, $a = 1.034$, and the tolerance boundary is defined as $\mathcal{Q} = 1e-4$. Figure 3 shows the wind profile within the speed range of 3.8-5.8 m/s with an average speed of 5.2 m/s. Figure 4 shows a comparative illustration of rotor speed tracking. It can be seen from Fig. 4 that all three applied methods demonstrate a similar tracking performance. Nonetheless, the zoomed-in insets reveal the superior performance of the proposed SMO-AFTSMC approach, providing more accurate trajectory tracking performance. Furthermore, a substantial reduction in tracking error with the proposed scheme compared to other methods can be observed, indicating its superior performance.

Figures 5 and 6 depict the performance of the developed SMO through rotor current dynamics estimation and reconstruction in the presence of lumped uncertainties and faulty sensors. As observed from Figs. 5 and 6, the estimation and reconstruction of $\mathcal{I}_{dr}$ and $\mathcal{I}_{qr}$ are accomplished with minimal error in a brief time, demonstrating its exceptional performance. In addition, the provided comparisons with the algebraic state observer (ASE) [20] demonstrate the superiority of the developed SMO with less estimation error.

Figure 7 illustrates the grid's active and reactive power tracking performances. Accordingly, it can be seen that all the control schemes have successfully carried out the grid active power tracking. However, as clearly seen from the zoomed-in insets, with a small transient response and a precise power tracking performance, the proposed SMO-AFTSMC has delivered a more improved power factor with superior reactive power regulation, surpassing the ASE-FTSMC and FSMC approaches. Figure 8 depicts the comparative sliding surfaces of the current and speed FSMC and FTSMC controllers. In this sense, although the sliding surfaces of both controllers are bounded,

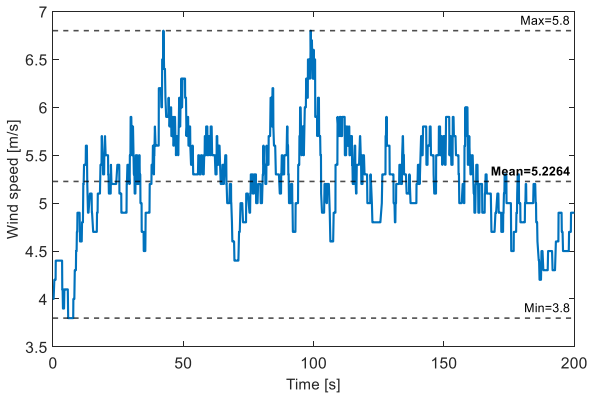

Figure 3: Wind speed profile.

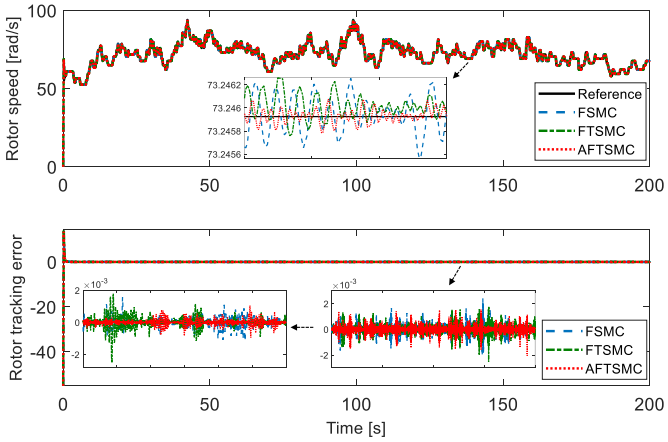

Figure 4: Comparative rotor speed tracking.

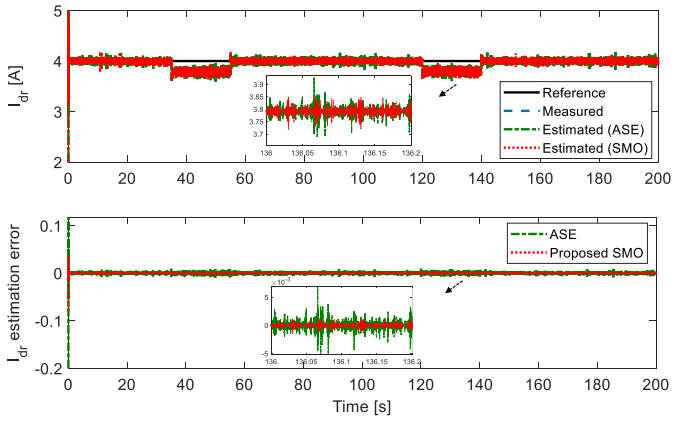

Figure 5: Comparative estimation of the rotor current I_{dr}.

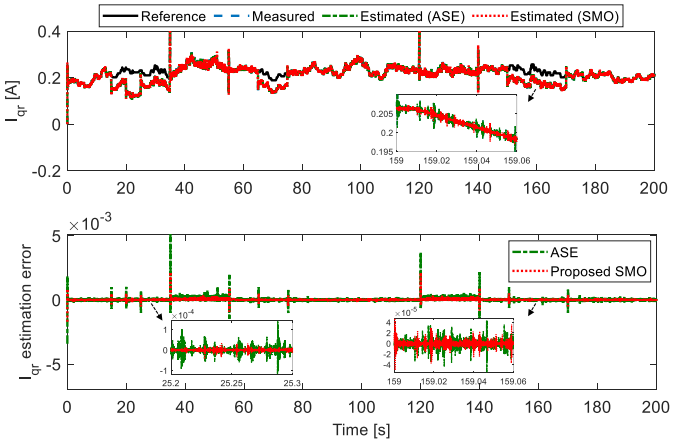

Figure 6: Comparative estimation of the rotor current I_{qr}.

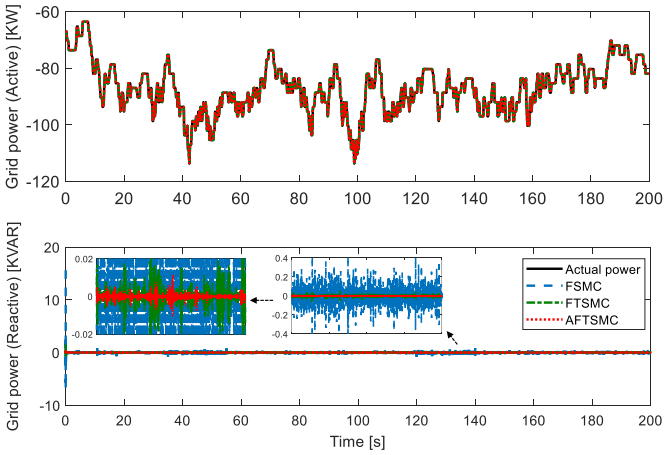

Figure 7: Active and reactive power tracking.

the proposed AFTSMC provides better chattering mitigation compared to the FSMC. From the obtained foregoing results, it is evident that the developed SMO delivered superior performance than the ASE observer. In addition, compared with the FSMC approach, the proposed fault-tolerant control paradigm offers superior performance in speed and power tracking.

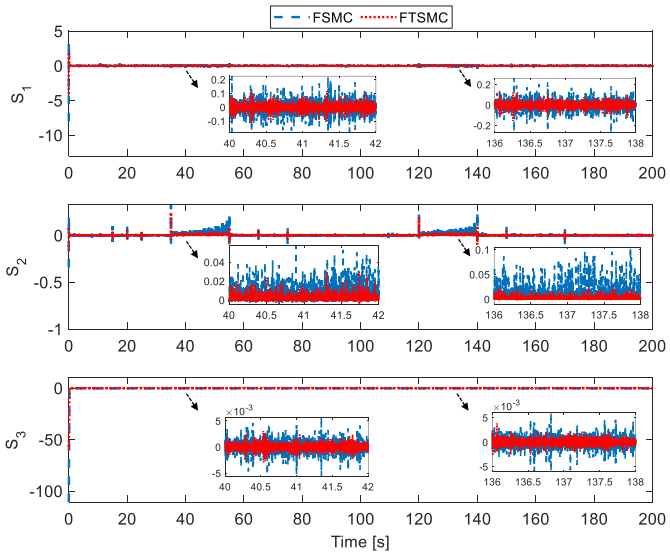

Figure 8: Comparative current and speed controllers' sliding surfaces.

6 Conclusion

Active and reactive power control of DFIG-based WECSs subjected to model uncertainties and sensor faults has been investigated in this work through a compound fault-tolerant control scheme. Two AFTSMC approaches with mitigated chattering and guaranteed finite-time convergence have been put forward to simultaneously deal with rotor current regulation and speed trajectory tracking problems. This work has also developed a robust sliding mode observer (SMO) to estimate and reconstruct the rotor current during sensor faults. The developed SMO has been incorporated with a tolerance limit to distinguish false fault detections and allow the SMO to detect actual faults occurrence and deliver highly reliable performance. According to the performance investigations in the presence of sensor faults, the augmentation of the proposed AFTSMC controllers and SMO demonstrated an outstanding fault-tolerant control analogous to the faultless case. Moreover, the comparative investigations with fractional-order SMC and algebraic state observer-based FTSMC revealed the developed method's remarkable power and speed tracking performance with mitigated chattering.

References

[1] F. Cheng, J. Wang, L. Qu, and W. Qiao, "Rotor-current-based fault diagnosis for dfig wind turbine drivetrain gearboxes using frequency analysis and a deep classifier," *IEEE transactions on industry applications*, vol. 54, no. 2, pp. 1062–1071, 2017.

[2] Y. Mousavi, G. Bevan, I. B. Kucukdemiral, and A. Fekih, "Sliding mode control of wind energy conversion systems: Trends and applications," *Renewable and Sustainable Energy Reviews*, vol. 167, p. 112734, 2022.

[3] R. Patel, F. Hafiz, A. Swain, and A. Ukil, "Nonlinear rotor side converter control of dfig based wind energy system," *Electric Power Systems Research*, vol. 198, p. 107358, 2021.

[4] P. Srinivasan and P. Jagatheeswari, "Machine learning controller for dfig based wind conversion system." *Intelligent Automation & Soft Computing*, vol. 35, no. 1, 2023.

[5] M. N. Musarrat and A. Fekih, "Event-triggered robust control scheme for subsynchronous resonance mitigation in dfig-based wecs," *International Journal of Electrical Power & Energy Systems*, vol. 148, p. 109006, 2023.

[6] B. Yang, L. Jiang, L. Wang, W. Yao, and Q. Wu, "Nonlinear maximum power point tracking control and modal analysis of dfig based wind turbine," *International Journal of Electrical Power & Energy Systems*, vol. 74, pp. 429–436, 2016.

[7] C. Cheng and H. Nian, "Low-complexity model predictive stator current control of dfig under harmonic grid voltages," *IEEE Transactions on Energy Conversion*, vol. 32, no. 3, pp. 1072–1080, 2017.

[8] X. Kong, X. Wang, M. A. Abdelbaky, X. Liu, and K. Y. Lee, "Nonlinear mpc for dfig-based wind power generation under unbalanced grid conditions," *International Journal of Electrical Power & Energy Systems*, vol. 134, p. 107416, 2022.

[9] K. A. Naik, C. P. Gupta, and E. Fernandez, "Design and implementation of interval type-2 fuzzy logic-pi based adaptive controller for dfig based wind energy system," *International Journal of Electrical Power & Energy Systems*, vol. 115, p. 105468, 2020.

[10] A. Merabet, H. Eshaft, and A. A. Tanvir, "Power-current controller based sliding mode control for DFIG-wind energy conversion system," *IET Renewable Power Generation*, vol. 12, no. 10, pp. 1155–1163, 2018.

[11] P. Li, L. Xiong, F. Wu, M. Ma, and J. Wang, "Sliding mode controller based on feedback linearization for damping of sub-synchronous control interaction in DFIG-based wind power plants," *International Journal of Electrical Power & Energy Systems*, vol. 107, pp. 239–250, 2019.

[12] Z. Huo and B. Wang, "Distributed resilient multi-event cooperative triggered mechanism based discrete sliding-mode control for wind-integrated power systems under denial of service attacks," *Applied Energy*, vol. 333, p. 120636, 2023.

[13] R. Venkateswaran, A. A. Yesudhas, S. R. Lee, and Y. H. Joo, "Integral sliding mode control for extracting stable output power and regulating dc-link voltage in pmvg-based wind turbine system," *International Journal of Electrical Power & Energy Systems*, vol. 144, p. 108482, 2023.

[14] R. Subramaniyam and Y. H. Joo, "Memory-based ismc design of dfig-based wind turbine model via t-s fuzzy approach," *IET Control Theory & Applications*, vol. 15, no. 3, pp. 348–359, 2021.

[15] K. Palanimuthu, H. S. Kim, and Y. H. Joo, "Ts fuzzy sliding mode control for double-fed induction generator-based wind energy system with a membership function-dependent h_∞-approach," *Information Sciences*, vol. 596, pp. 73–92, 2022.

[16] L. Djilali, E. N. Sanchez, and M. Belkheiri, "Real-time neural sliding mode field oriented control for a dfig-based wind turbine under balanced and unbalanced grid conditions," *IET Renewable Power Generation*, vol. 13, no. 4, pp. 618–632, 2019.

[17] X. Yin, Z. Jiang, and L. Pan, "Recurrent neural network based adaptive integral sliding mode power maximization control for wind power systems," *Renewable Energy*, vol. 145, pp. 1149–1157, 2020.

[18] Y. Mousavi, G. P. Bevan, I. B. Kucukdemiral, and A. Fekih, "Maximum power extraction from wind turbines using a fault-tolerant fractional-order nonsingular terminal sliding mode controller," *Energies*, 2021.

[19] Y. Dong, J. Wang, S. Ding, and W. Li, "Adaptive fractional-order fault-tolerant sliding mode control scheme of dfig wind energy conversion system," *Proceedings of the Institution of Mechanical Engineers, Part I: Journal of Systems and Control Engineering*, vol. 237, no. 1, pp. 15–25, 2023.

[20] Y. Mousavi, G. Bevan, I. B. Kucukdemiral, and A. Fekih, "Active fault-tolerant fractional-order terminal sliding mode control for dfig-based wind turbines subjected to sensor faults," in *IEEE IAS Global Conference on Emerging Technologies (GlobConET'22)*. IEEE, 2022.

[21] G. Tu, Y. Li, and J. Xiang, "Sliding mode control of energy storage systems for reshaping the accelerating power of synchronous generators," *IEEE Transactions on Power Systems*, 2022.

[22] N. Ullah, M. A. Ali, A. Ibeas, and J. Herrera, "Adaptive fractional order terminal sliding mode control of a doubly fed induction generator-based wind energy system," *IEEE Access*, vol. 5, pp. 21 368–21 381, 2017.

[23] R. Patnaik and P. Dash, "Fast adaptive finite-time terminal sliding mode power control for the rotor side converter of the DFIG based wind energy conversion system," *Sustainable Energy, Grids and Networks*, vol. 1, pp. 63–84, 2015.

[24] A. Merabet, K. T. Ahmed, H. Ibrahim, and R. Beguenane, "Implementation of sliding mode control system for generator and grid sides control of wind energy conversion system," *IEEE Transactions on Sustainable Energy*, vol. 7, no. 3, pp. 1327–1335, 2016.

[25] J. Hussain and M. K. Mishra, "An efficient wind speed computation method using sliding mode observers in wind energy conversion system control applications," *IEEE Transactions on Industry Applications*, vol. 56, no. 1, pp. 730–739, 2019.

[26] U. Abubakar, S. Mekhilef, K. S. Gaeid, H. Mokhlis, and Y. I. Al Mashhadany, "Induction motor fault detection based on multi-sensory control and wavelet analysis," *IET Electric Power Applications*, vol. 14, no. 11, pp. 2051–2061, 2020.

[27] B. Yang, L. Zhong, T. Yu, H. Shu, P. Cao, N. An, Y. Sang, and L. Jiang, "Pc-smc design of permanent magnetic synchronous generator for maximum power point tracking," *IET Generation, Transmission & Distribution*, vol. 13, no. 14, pp. 3115–3126, 2019.

[28] G. Mamani, J. Becedas, V. Feliu-Batlle, and H. Sira-Ramırez, "An algebraic state estimation approach for DC motors," in *Proceedings of the World Congress on Engineering and Computer Science 2007 WCECS 2007*. Citeseer, 2007.

[29] P. Li, J. Wang, L. Xiong, M. Ma, Z. Wang, and S. Huang, "Mitigating subsynchronous control interaction using fractional sliding mode control of wind farm," *Journal of the Franklin Institute*, vol. 357, no. 14, pp. 9523–9542, 2020.

[30] M. N. Musarrat, A. Fekih, and M. R. Islam, "An improved fault ride through scheme and control strategy for DFIG-based wind energy systems," *IEEE Transactions on Applied Superconductivity*, vol. 31, no. 8, pp. 1–6, 2021.

[31] H. Kim, J. Son, and J. Lee, "A high-speed sliding-mode observer for the sensorless speed control of a pmsm," *IEEE transactions on Industrial Electronics*, vol. 58, no. 9, pp. 4069–4077, 2010.

[32] J. E. Gentle, "Matrix algebra," *Springer texts in statistics, Springer, New York, NY, doi*, vol. 10, pp. 978–0, 2007.